Synthesis and characterization of $NaYF_4:Pr^{3+}$@$NaYF_4:Eu^{3+}$ core@shell nanoparticles as down-conversion material for organic solar cells application

Prerna Mahajan[1], Anoop Singh[1,2], Ram Datt[3], Wing Chung Tsoi[3], Vinay Gupta[4], and Sandeep Arya[1,#]

[1]Department of Physics, University of Jammu, Jammu, J&K-180006, India

[2]Centre for Global Health Research, Saveetha Medical College and Hospitals, Saveetha Institute of Medical and Technical Sciences, Chennai 602105, Tamil Nadu, India

[3]SPECIFIC, College of Engineering, Swansea University Bay Campus, Fabian Way, SA18EN, Swansea, United Kingdom

[4]Department of Physics, Khalifa University of Science and Technology, Abu Dhabi, 127788,United Arab Emirates

[#]Corresponding author Email: snp09arya@gmail.com

Abstract

Here, a transparent luminescent down-conversion material (DCM) of $NaYF_4:Pr^{3+}$@$NaYF_4:Eu^{3+}$ core@shell nanoparticles has been used for OSCs application. The core@shell nanoparticles were prepared via a chemical sol-gel process. In OSCs, the prepared DCM is coated at backside of indium-doped tin oxide (ITO) glass substrate, and the final device is called optimized device, whereas the uncoated device is defined as control device. The power conversion efficiency (PCE) of optimized device improved from 7.95 to 8.45 %, as a result of the DCM re-emitting ultraviolet light in the visible range. Most importantly, the control device had inadequate stability under UV-B light, and within 90 minutes, efficiency has decreased by 38%. However, optimized device shows significantly superior performance by maintaining 84% of its initial PCE even after 90 minutes. It has been suggested that the $NaYF_4:Pr^{3+}$@$NaYF_4:Eu^{3+}$ DCM minimizes the ultraviolet deterioration while also improving the PCE of OSCs.

Keywords

Sol-gel, core@shell, nanoparticles, organic solar cell, down-conversion.

1. Introduction

The need for energy is becoming the lifeblood of modern human existence. Household equipment, communication, transportation, industry, and economic expansion are all powered by energy [1]. Global energy consumption and carbon emissions are increasing, with estimates that both will double in 2050 compared to 2001 levels [2]. Energy supplies are becoming depleted as we become more reliant on fossil fuels, whose inventories are finite, and society must consider alternatives [3]. Sunlight is the most plentiful and environmentally friendly source of energy that can be readily transformed into electricity using solar cells. Moreover, this renewable energy source maintains the environmental safety [4]. Organic solar cells (OSCs) in photovoltaic technology have recently come out as flexible, solution processable, cost effective, and showed comparable performance to existing inorganic photovoltaic technologies [5-7]. OSCs have received tremendous attention of the scientific community and corporate since it is projected to be a cost-effective and sustainable source of energy and recently its PCE crossed the barrier of 20% [8].

It is extremely important to develop stable photovoltaic devices for future commercial applications as material engineering could deliver a promising strategy to achieve it. Air and moisture shield can be achieved by encapsulation, but still, the presence of UV-light-induced degradation can reduce the durability and efficiency of the OSCs. Photo degradation in OSCs, especially UV-induced, can impact a variety of layers rather than simply the photoactive layer [9]. The application of UV-Cut Filter (UCF) can guard them from UV-irradiation, but the overall incident light intensity decreased and reduces the OSCs performance, and also does not provide any other benefit. The reduced stability of OSCs under ultraviolet light is caused by the oxidative degradation of constitute materials in photoabsorber layers and formation of $PC_{71}BM$ aggregates [10]. Moreover, the researchers are switching to non-fullerene acceptors in place of the fullerene derived that helped to attain a higher performance of OSCs. Despite all these approaches, the solar spectral mismatch-based issue could not be resolved, which is undoubtedly an important reason for the limited efficiency of OSCs.

Recently, spectral conversion materials have been introduced into photovoltaic for assisting the conversion of photons energy from high to low and vice-versa, known as down-conversion (DC) and up-conversion (UC) process, respectively [11,12]. The DC mechanism could probably aid in resolving the issue of UV induced degradation in OSCs, thereby

enhancing its efficiency. The maximum efficiency of solar cells is theoretically calculated as 30% at 1.1 eV bandgap while considering the radiative recombination and is expressed as Shockley and Queisser limit of efficiency [13]. The thermalization process caused by high-energy photon absorptions and non-absorption of low-energy photons cause fundamental losses in solar cells. This is known as a spectral mismatch between the incident solar spectrum and the absorption profile of the solar cell. The efficiency of conventional solar cells may be improved by utilizing luminescence spectrum converters, and it may even reach the Shockley and Queisser limit for non-concentrated sunlight with the same radiative recombination assumption [14].

The materials named as down-conversion materials (DCMs) exhibit the down-conversion (DC) phenomenon that converts a photon of high energy into a photon of lower energy [15]. Lanthanides are the prevalent materials as DCMs in OSCs for spectral conversion and in recent times, mixed lanthanide materials like core@shell materials and composite nanophosphors, are also being investigated as DCMs. These DCMs have been shown to boost the efficiency and stability of OSCs when exposed to UV radiation [16]. However, DCMs were first used in luminous devices like plasma discharge panels and fluorescent tubes, and they have recently been investigated for use in solar cells to absorb the unutilized higher energy photons and also help in minimizing the thermalization losses of electron-hole pairs [17]. The DC mechanism was originally studied in single lanthanide ions like Tm^{3+} and Gd^{3+}, and then in two-ion systems like Gd^{3+}- Eu^{3+} and Tb^{3+}-Yb^{3+}, etc., where one material (donor) ion transmits the excited energy sequentially to two other material (acceptor) ions. There is currently minimal research on the use of lanthanide-based core@shell DCMs for OSCs to improve photovoltaic performance. The introduction of $NaYF_4:Pr^{3+}$@$NaYF_4:Eu^{3+}$ core@shell nanoparticles as a DCM material has been proposed in this work. The DCM material is synthesized at different ratio of praseodymium (Pr) and Europium (Eu), and denoted as C, D, E samples. Sample C is applied in the OSCs as DCM material, and it improved the device performance as well as stability under UV-B light. The photocurrent density was the main parameter which improved. Furthermore, DCM showed high impact on improving OSC device stability under UV-B light.

2. Experimental Section

2.1. Synthesis of core ($NaYF_4:Pr^{3+}$)

Yttrium oxide (Y_2O_3), praseodymium (III) sulfate ($Pr_2(SO_4)_3$), sodium fluoride (NaF) and hydrochloric acid (HCl) were taken as elementary materials for synthesizing $NaYF_4:Pr^{3+}$ nanoparticles as core. 3.246 g of Y_2O_3 in 48 ml HCl and 0.012 g of $Pr_2(SO_4)_3$ in 12 ml HCl were dissolved at fixed temperature with constant stirring in two separate beakers. The clear homogenous solutions were mixed together, and 60 mL EDTA was added to the resultant solution. To keep the pH at 2, ammonia was added drop by drop. The resulting combination was then placed into a 180 ml NaF solution (6.3 g NaF in distilled water) that had been produced at the same time and agitated for 1 hour. Centrifugation was used to collect the nanocrystals, which were then washed with deionized water and ethanol numerous times before being dried in a 90 °C oven.

2.2. Shelling of $NaYF_4:Pr^{3+}$ with $NaYF_4:Eu^{3+}$

The shelling of $NaYF_4:Eu^{3+}$ on $NaYF_4:Pr^{3+}$ was done by taking Yttrium oxide (Y_2O_3), europium oxide (Eu_2O_3), sodium fluoride (NaF) and hydrochloric acid (HCl) as precursors. 2.164 g of Y_2O_3 in 32 ml HCl and 0.008 g of Eu_2O_3 in 8 ml HCl were dissolved at fixed temperature with constant stirring in two separate beakers. The clear homogenous solutions were mixed together, and 40 mL EDTA was added to the resultant solution. To keep the pH at 2, ammonia was added drop by drop. The resulting combination was then placed into a 120 ml NaF solution (4.2 g NaF in distilled water) that had been made at the same time and agitated for 1 hour. Other two solutions are made similarly, with Eu_2O_3 concentrations of 0.016 and 0.032 g, respectively, with the concentrations of NaF, HCl, and EDTA remaining constant. With constant stirring, the $NaYF_4:Eu^{3+}$ solution is poured into the beaker containing $NaYF_4:Pr^{3+}$. To avoid agglomeration, a mixture of ethanol and deionized water was added dropwise to the aforementioned solution. Finally, the nanocrystals were recovered by centrifugation, washed multiple times with deionized water and ethanol, and dried in an oven at 90 °C. Consequently, the desired core@shell nanoparticles of $NaYF_4:Pr^{3+}@NaYF_4:Eu^{3+}$ were obtained. In this study, three different samples of $NaYF_4:Pr^{3+}@NaYF_4:Eu^{3+}$ were prepared by taking different weights of precursors: Sample C (Eu_2O_3 =0.008 g), Sample D (Eu_2O_3 =0.016 g), and Sample E (Eu_2O_3 =0.032 g) while the concentration of $Pr_2(SO_4)_3$ was kept constant.

2.3 Device fabrication

For the fabrication of OSCs, the inverted device structure (ITO/ZnO/active layer/MoO_3/Ag) was used. Sample C was utilized as the DCM and two solutions of sample C

were prepared in solvent 2-Methoxyethanol to yield different concentrations (5 mg/ml and 10 mg/ml). The DCM solution was coated on the reverse side of ITO using spin coating at 800 rpm for 3 seconds, followed by 2000 rpm for 20 seconds. Thermal annealing was done at 180 °C for 30 minutes in ambient condition. ZnO was spin-coated over ITO at 4000 rpm for 40 seconds followed by thermal annealing at 150 °C for 10 minutes. The active layer PTB7-Th: $PC_{71}BM$ (1: 1.5, 25mg/ml in chlorobenzene with 3% diiodooctane) was spin-coated at 1200 rpm. Finally MoO_3 (10 nm) and Ag (100 nm) were deposited by thermal evaporation method. The devices were encapsulated.

3. Results and discussions

A Powder X-ray Diffractometer (XRD) was used to conduct crystallinity and structure investigation (Make: Rigaku Corporation). The Scanning Electron Microscope (SEM) images in this work were acquired utilizing powerful FESEM –EDX equipment (Make: JFEI firm of USA (S.E.A.) PTE LTD). Similarly, the presence of the elements in the produced samples was identified in the recent study utilizing energy dispersive X-ray analysis equipment connected to a Scanning Electron Microscope: FESEM –EDX (Make: JFEI firm of USA (S.E.A.) PTE LTD). A high-resolution transmission electron microscope (Make: USA FEI company) was utilized to conduct TEM measurements. The Raman Spectroscopy (Make: Horiba) technique was performed to study their surface chemistry. A 532 nm wavelength laser was used. The UV-Vis Spectrophotometer (Make: Shimadzu Corporation) was utilized to obtain the absorption spectra. Fluorescence Spectrometer (Make: Agilent Technologies) was used to conduct the photoluminescence (PL) research in the present work.

3.1 X-ray diffraction (XRD)

A monochromatic X-ray beam is incident on a sample, and the intensity of the reflected beam is measured in a standard XRD experiment. The X-rays are scattered at the sample's crystallographic lattice planes [18]. In order to verify the crystal structure as well as the phase purity of $NaYF_4:Pr^{3+}@NaYF_4:Eu^{3+}$ core@shell nanoparticles, structural examination of the samples was performed by XRD method in the angle range 2θ = 10° to 90° as shown in Fig. 1. The XRD graphs clearly show well-defined sharp peaks which are related to β-$NaYF_4$ at 20.65°, 23.08°, 28.11°, 29.31°, 33.81°, 40.41°, 43.7°, 46.67°, 48.6°, 53.04°, 55.3°, 57.91°, 68.56°, 75.09° and 77.9° and belong to the crystal planes (100), (001), (110), (101), (200), (111), (201), (210), (002), (300), (211), (102), (202), (311), and (302)

respectively. XRD peaks are in excellent accordance with the hexagonal crystal structure of β-$NaYF_4$ according to the JCPDS file 28-1192 [19]. As a result, the prepared $NaYF_4:Pr^{3+}@NaYF_4:Eu^{3+}$ core@shell nanoparticles are a single phased material. Furthermore, thorough study indicates that the relative diffraction peak strength of XRD patterns fluctuates with varied Pr^{3+} and Eu^{3+} molar ratios, indicating morphological development of as-prepared β-$NaYF_4$ nanocrystals.

From the graph, it is observed that with the increase in the dopant concentration, the dopant atoms may occupy lattice sites in the crystal structure, replacing host atoms. This can lead to a dilution of the host lattice, causing a reduction in the overall crystalline volume. The decrease in the number of host atoms participating in the diffraction process results in lower XRD peak intensities. Moreover, no extra peaks subsequent to other impurity crystalline phases were observed illustrating that the lanthanide ions have been effectively doped into the host lattices which indicate the purity of the sample. The production of nanometer-scale particles is confirmed by a distinct line broadening in the diffraction peaks.

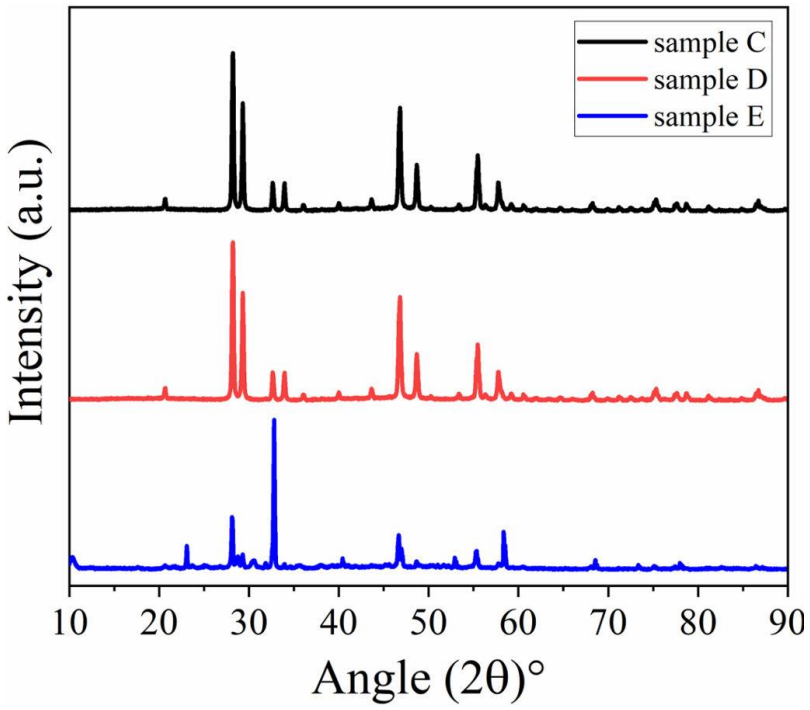

Fig. 1 XRD graph of the synthesized $NaYF_4:Pr^{3+}@NaYF_4:Eu^{3+}$ core@shell nanoparticles.

The Debye-Scherrer formula [20] was used to calculate the average crystallite size (D) based on peak broadening.

$$D = K\lambda/(\beta \cos\theta) \quad (1)$$

where λ equals 1.5406 Å (wavelength of the X-ray employed), K =0.9, is the dimensionless shape factor, and β is the full-width half maximum (FWHM) value, and θ is the Bragg angle (in degrees). Cu-Kα radiation with a wavelength of 1.5406 Å was used for the XRD observations. The average crystallite sizes of produced nanoparticles were observed as 65 nm, 74 nm and 73 nm for sample C, D and E, respectively.

3.2 Scanning electron microscopy (SEM)

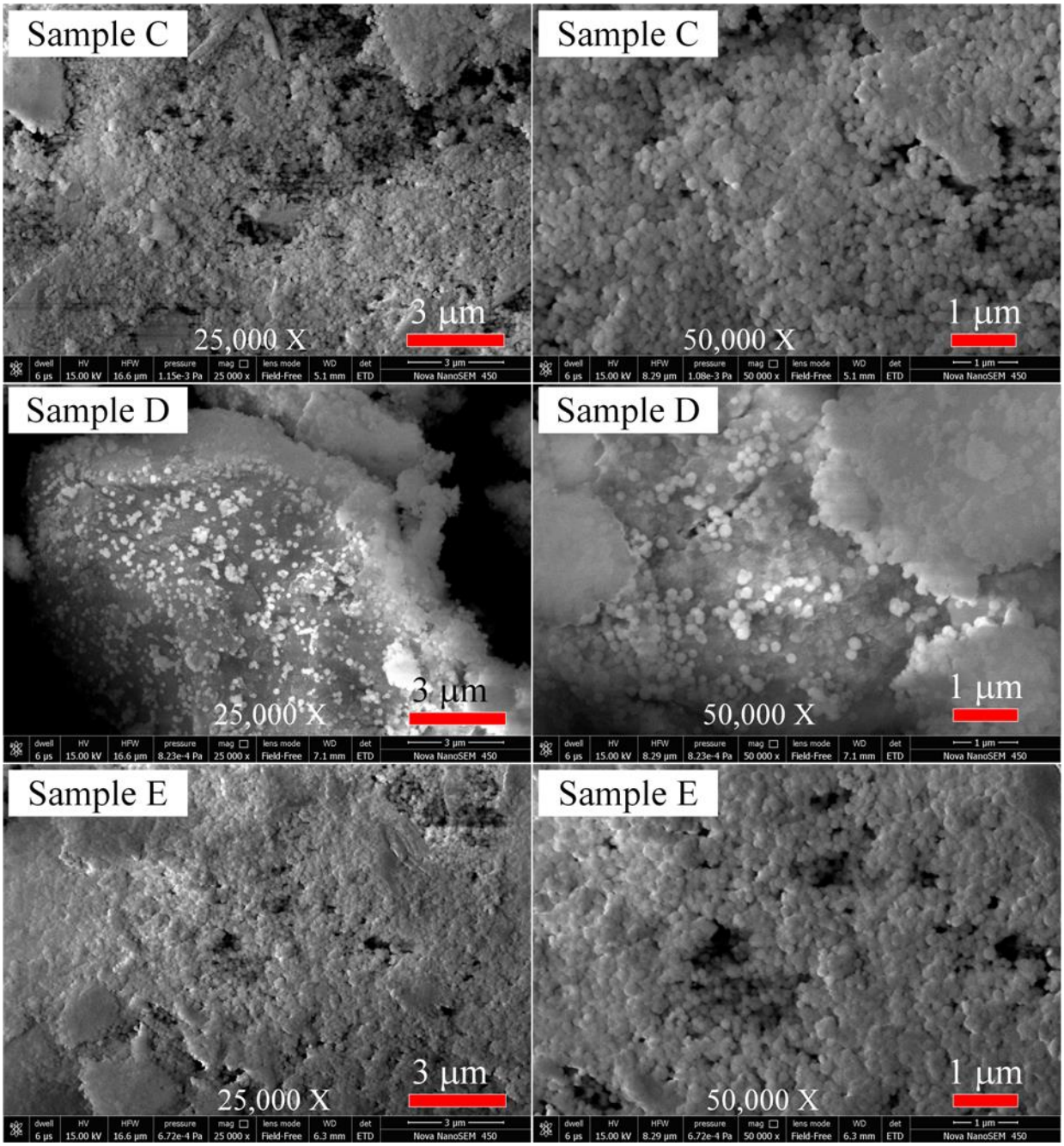

Fig. 2 SEM images of the synthesized $NaYF_4:Pr^{3+}@NaYF_4:Eu^{3+}$ core@shell nanoparticles at different magnifications.

SEM is a surface method that is basically intended to capture pictures of three-dimensional objects on the surfaces of specimens [21]. SEM was used to examine the morphology of the produced $NaYF_4:Pr^{3+}@NaYF_4:Eu^{3+}$ core@shell nanoparticles that illustrates the influence of $NaYF_4:Eu^{3+}$ shelling onto $NaYF_4:Pr^{3+}$ nanoparticles. The resulting SEM pictures of samples C, D and E at different magnifications are depicted in Fig. 2. The pictures showed nanoparticle-with roughly spherical morphology. Moreover, agglomeration occurred, and the nanoparticles are held together. Some large size grains were also present revealing that complete separation is not acquired. This may be the consequence of higher surface area as well as surface energy of nanoparticles. Due to increasing surface area to volume ratio, attractive physical forces exist between particles that led to the agglomeration of nanoparticles [22]. Furthermore, the observed size of the synthesized $NaYF_4:Pr^{3+}@NaYF_4:Eu^{3+}$ core@shell nanoparticles as seen in the SEM picture agrees well with particle size calculated using the Debye-Scherrer formula. The synthesis of $NaYF_4:Pr^{3+}@NaYF_4:Eu^{3+}$ core@shell nanoparticles is successfully acquired in nanometer range.

3.3 Energy dispersive X-ray spectroscopy (EDX)

The EDX results of the $NaYF_4:Pr^{3+}@NaYF_4:Eu^{3+}$ core@shell nanoparticles of samples C, D and E are illustrated in Fig. 3, Fig. 4, and Fig. 5, respectively. The enclosed table shows the percentages (atomic and weight) of the elements contained in the samples. During EDX analysis, a very less amount of sample is required. Therefore, there is always some uncertainty in the values obtained as observed in the present analysis, which is due to the lack of Europium content in that area under scan. The dopant might not be uniformly distributed throughout the material. This can happen if the manufacturing or doping process is not well-controlled, resulting in localized regions with higher dopant concentration.

The EDX spectra show that sodium, yttrium, fluorine, praseodymium and europium are present in all the samples of $NaYF_4:Pr^{3+}@NaYF_4:Eu^{3+}$ core@shell nanoparticles. For sodium and fluorine, K emission peak appears, whereas L emission peak is seen in case of yttrium, praseodymium and europium. As a result, EDX showed well-defined peaks with no impurity phase. Additionally, elemental mapping of the produced nanoparticles has been demonstrated along with the spectra. In general, the results reveal that the products include no other element apart from five elements sodium, yttrium, fluorine, praseodymium and

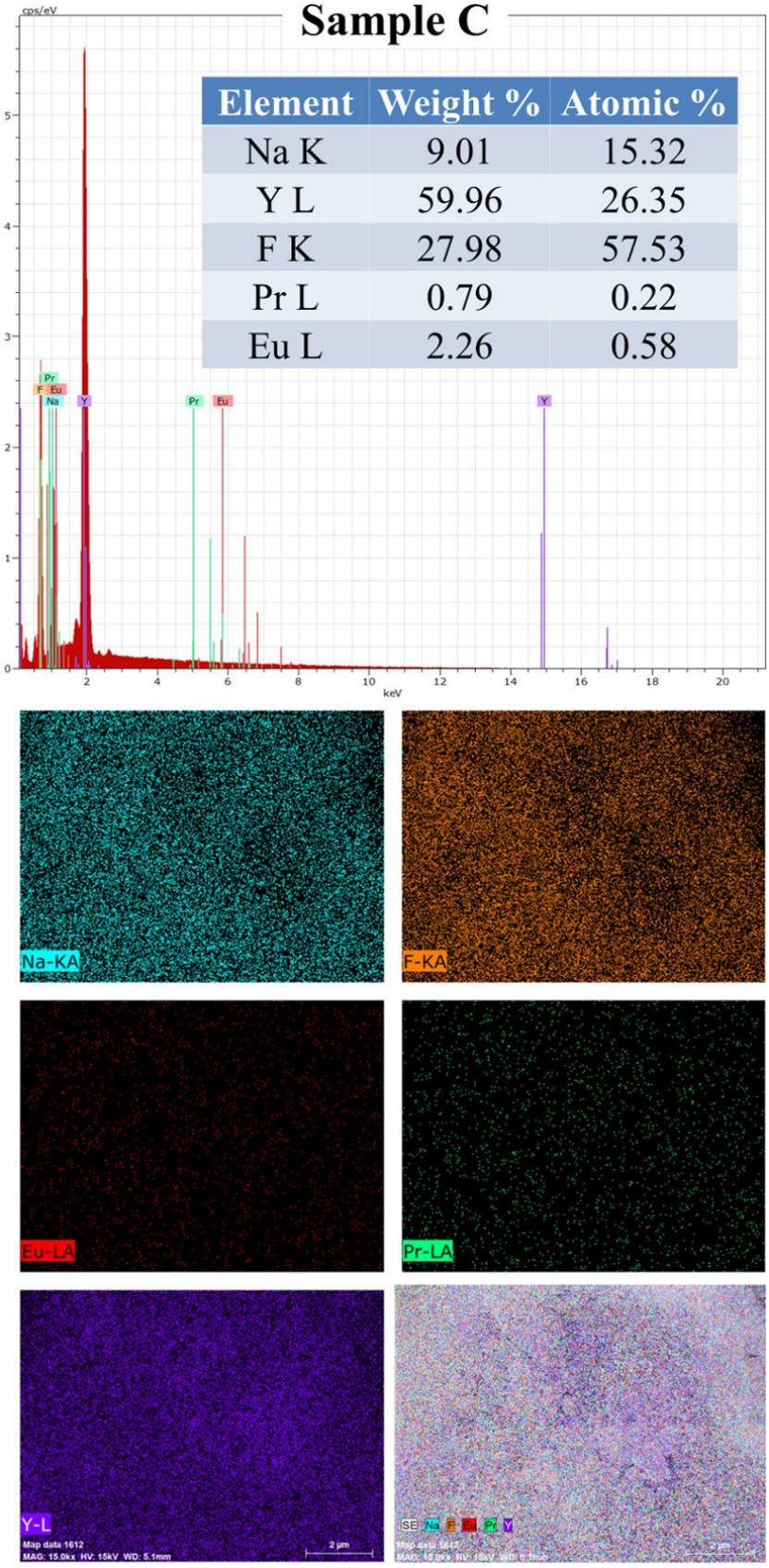

europium enlightening that the prepared samples are highly pure. The XRD result was validated and corroborated by EDX findings, indicating that the desired materials we re successfully produced using the sol-gel approach.

Fig. 3 EDX spectra and elemental mapping of sample C of $NaYF_4:Pr^{3+}$ @$NaYF_4:Eu^{3+}$ core@shell nanoparticles.

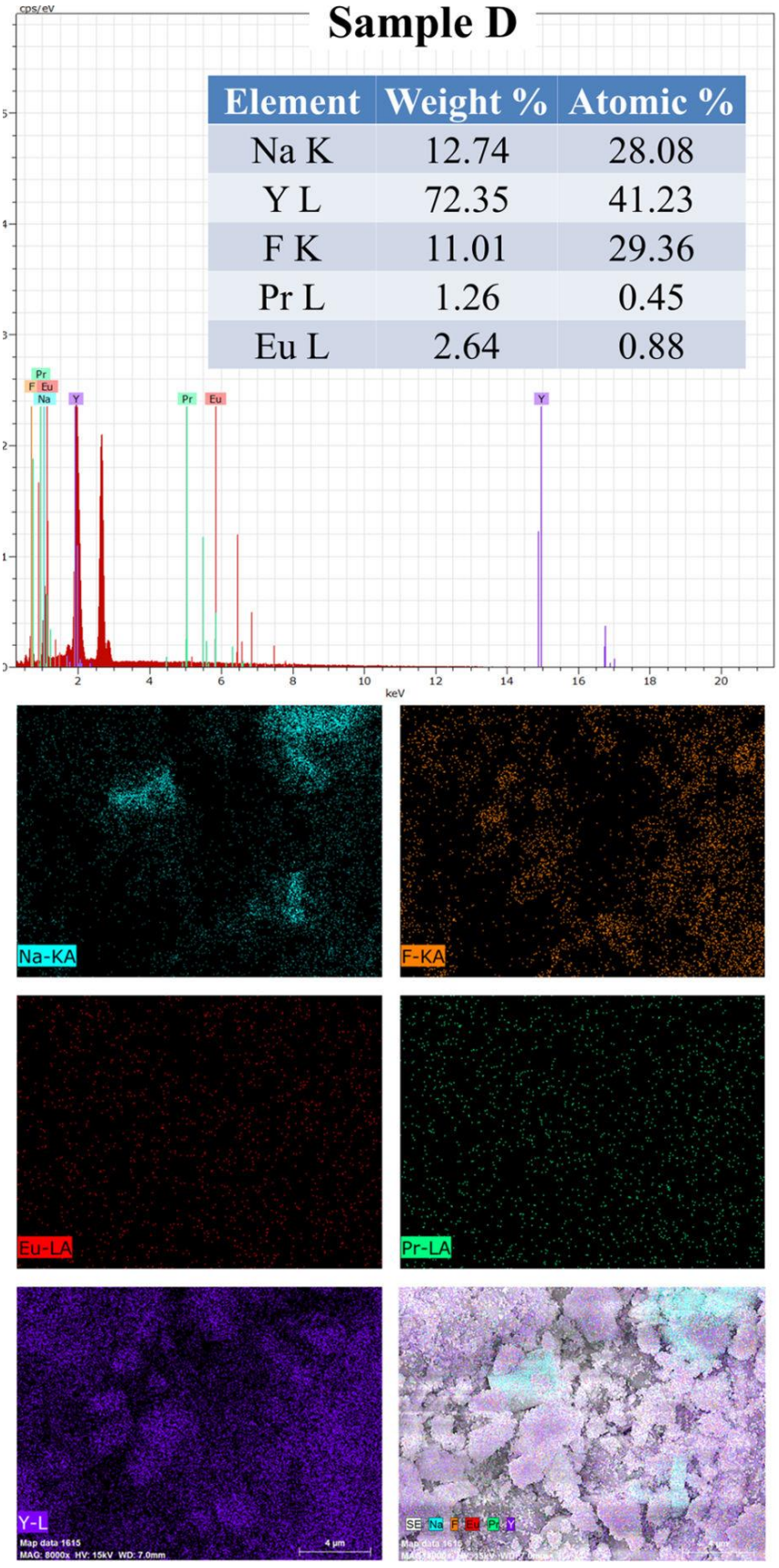

Fig. 4 EDX spectra and elemental mapping of sample D of $NaYF_4:Pr^{3+}@NaYF_4:Eu^{3+}$ core@shell nanoparticles.

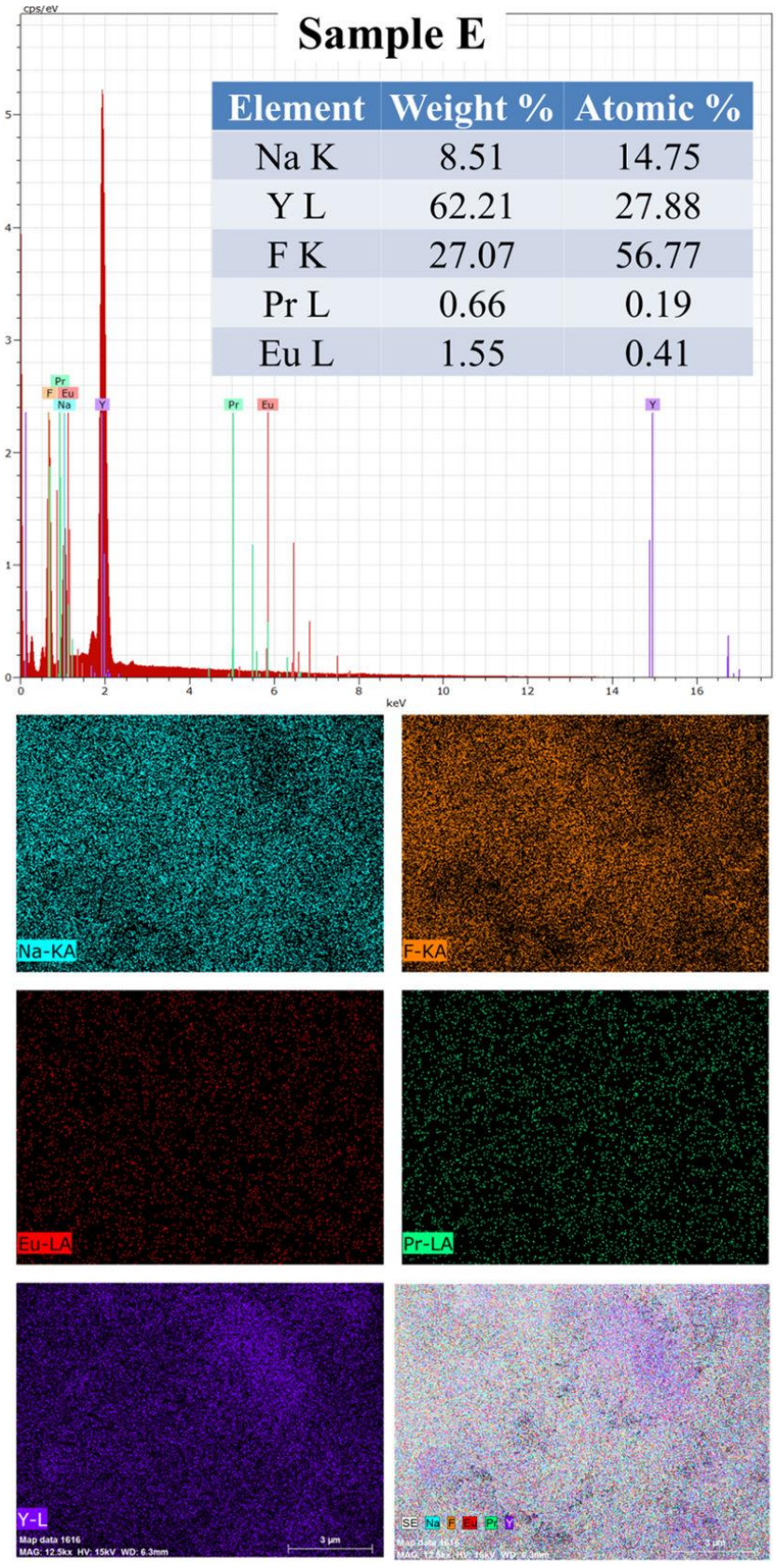

Fig. 5 EDX spectra and elemental mapping of sample E of $NaYF_4:Pr^{3+}@NaYF_4:Eu^{3+}$ core@shell nanoparticles.

3.4 Transmission electron microscopy (TEM)

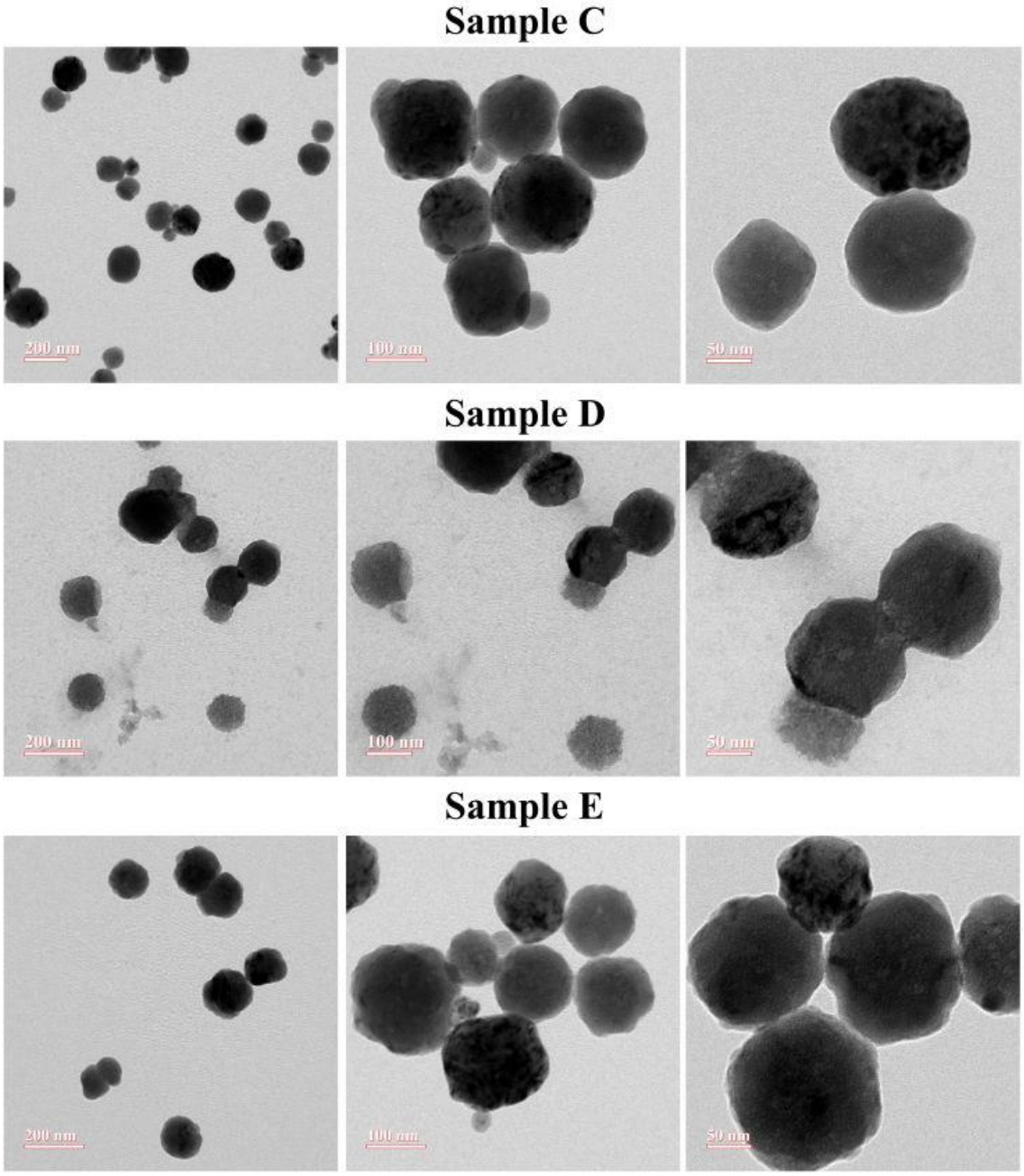

Fig. 6 TEM pictures of prepared $NaYF_4:Pr^{3+}@NaYF_4:Eu^{3+}$ core@shell nanoparticles at different magnifications.

For verifying the morphology and to validate more accurately the size of the produced $NaYF_4:Pr^{3+}@NaYF_4:Eu^{3+}$ core@shell nanoparticles, High Resolution-TEM was undertaken. The resulting images of samples C, D and E at different magnifications have been demonstrated in Fig. 6. The morphology of the sample showed that the synthesized particles are in nanometer scale i.e., less than 100 nm. A nanostructure with a core of $NaYF_4:Pr^{3+}$ and a

shell of $NaYF_4:Eu^{3+}$ is seen in the TEM microphotograph. The particle size (60-80 nm) produced is clearly in good accord with XRD measurement findings. Secondly, the densities of $NaYF_4:Pr^{3+}$ and $NaYF_4:Eu^{3+}$ vary, making it easier to distinguish between the two. The lighter portion is $NaYF_4:Eu^{3+}$, whereas the darker portion is $NaYF_4:Pr^{3+}$. This strongly suggests that a homogeneous layer of $NaYF_4:Eu^{3+}$ forms over the $NaYF_4:Pr^{3+}$ surface. Furthermore, the images prove the formation of nanoparticles with well-defined spherical shape.

3.5 Raman analysis

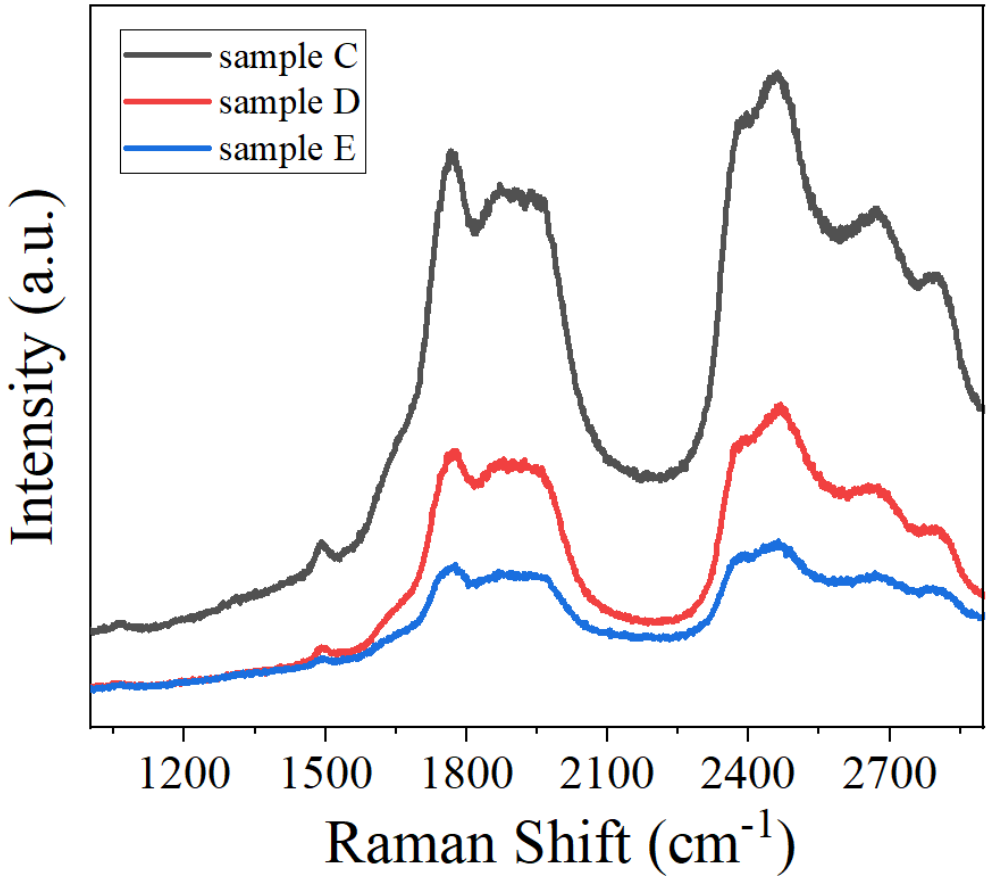

Fig. 7 Raman spectra of $NaYF_4:Pr^{3+}$@$NaYF_4:Eu^{3+}$ core@shell nanoparticles.

Raman spectroscopy is utilized to characterize the structural changes caused by the $NaYF_4:Eu^{3+}$ coating on $NaYF_4:Pr^{3+}$and the Raman spectra of the generated samples C, D and E of $NaYF_4:Pr^{3+}$@$NaYF_4:Eu^{3+}$ core@shell nanoparticles are shown in Fig. 7. Two broad bands were observed in the ranges 1764-1959 cm^{-1} and 2370-2500 cm^{-1} for all the samples that have been ascribed to the host lattice $NaYF_4$ vibrational features [23]. The Raman spectra for the three samples show different peak heights for samples C, D and E. Raman intensities

decrease as particle size increases. We observed that the particle size increased for the synthesized sample with increase in doping. That's why the Raman intensity of sample D is lower than sample C and that of sample E is the lowest. Furthermore, the spectra show no additional impurity peak which is consistent with XRD and EDX data.

3.6 PL characterization

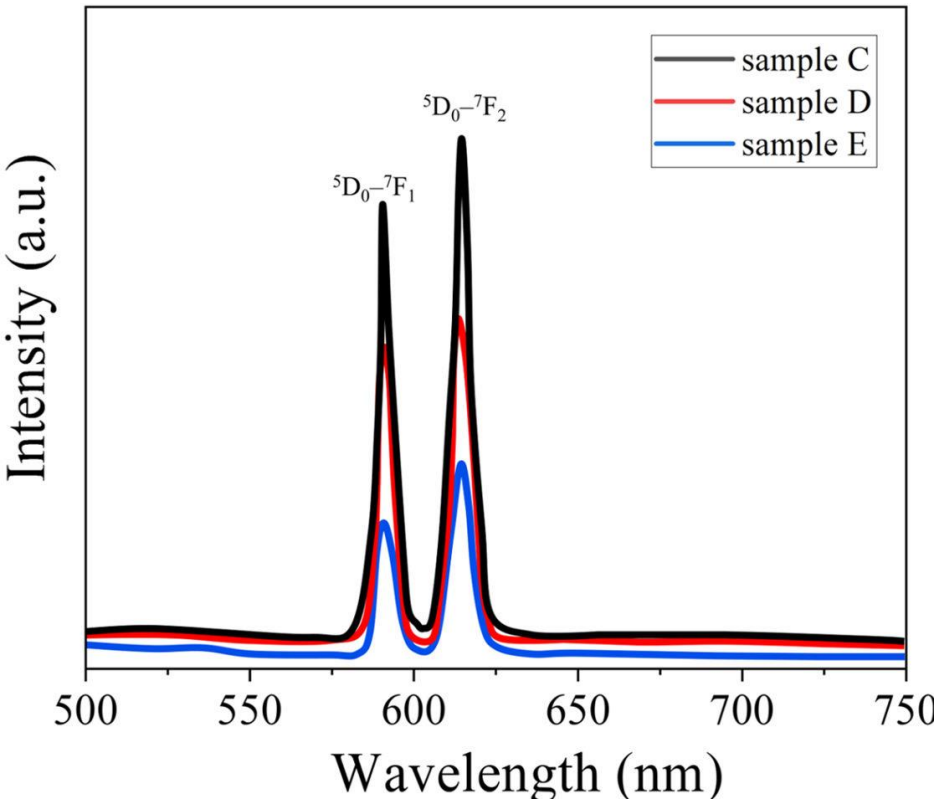

Fig. 8 PL spectra of the synthesized $NaYF_4:Pr^{3+}$@$NaYF_4:Eu^{3+}$ core@shell nanoparticles.

Photoluminescence (PL) spectroscopy is an important method for studying material optical characteristics [24]. The material absorbs the incoming photons and transfers extra energy through a photo excitation process in which electrons inside the substance travel to permissible excited states in this non-destructive and contactless technique. Surplus energy is emitted when returning to equilibrium states, and that can be radiative or non-radiative. The energy difference between the two electron states involved in the transition between the excited and equilibrium states is proportional to the emitted light energy in the radiative process [25]. As a result, room temperature photoluminescence spectra for the produced $NaYF_4:Pr^{3+}$@$NaYF_4:Eu^{3+}$ core@shell nanoparticles were obtained in order to investigate the optical characteristics of nanoparticles, as shown in Fig. 8. The produced core@shell nanoparticles' down-conversion luminescence spectra were collected with an excitation

wavelength of 275 nm in the ultraviolet range. The objective of developing core@shell nanoparticles was to optimize the photoluminescence quantum yield while reducing the concentration quenching effect, hence $NaYF_4:Eu^{3+}$ was shelled over $NaYF_4:Pr^{3+}$ core. Since the nanoparticles of core $NaYF_4:Pr^{3+}$ are roughly 40 nm in size, the surface effects (due to ligands, solvents, and surface defects, etc. considerably suppressed the photoluminescence of luminous Pr^{3+} ions, as a major fraction of the Pr^{3+} ions would have been present near the particle surface [26]. Pr^{3+} ions are adequately protected from surface quenchers by the layer of shell $NaYF_4:Eu^{3+}$. Transfer of energy from host material as well as from some other ion with a greater absorption coefficient might lead to significantly improved luminescence efficiency [27].

At 275 nm excitation, the spectra of $NaYF_4:Pr^{3+}@NaYF_4:Eu^{3+}$ core@shell nanoparticles revealed two distinct peaks, both of which are in visible range. The $^5D_0–^7F_1$ transitions of europium are responsible for strong peaks at 589 nm. Transitions between $^5D_0$ and $^7F_2$ produced further prominent peaks at 614 nm [28]. Due to optimum excitation of $NaYF_4:Pr^{3+}@NaYF_4:Eu^{3+}$ core@shell nanoparticles at about 275 nm, yellow emission was achieved for the peak centred at 589 nm and orange emission for the peak centred at 614 nm. It was discovered that Eu-dopant, when used as an efficient down-conversion material in the produced sample, could convert ultraviolet light into visible light and aid to widen the absorption spectrum of OSCs. Additionally, it was observed that the PL peak intensity decreases when the Eu concentration in the samples increases. This is due to the fact of concentration quenching. Concentration quenching occurs when the concentration of dopant ions increases, leading to a decrease in the efficiency of the radiative recombination process responsible for PL. This is often due to the saturation of available radiative recombination centers.

3.7 Ultraviolet-visible (UV-Vis) spectroscopy

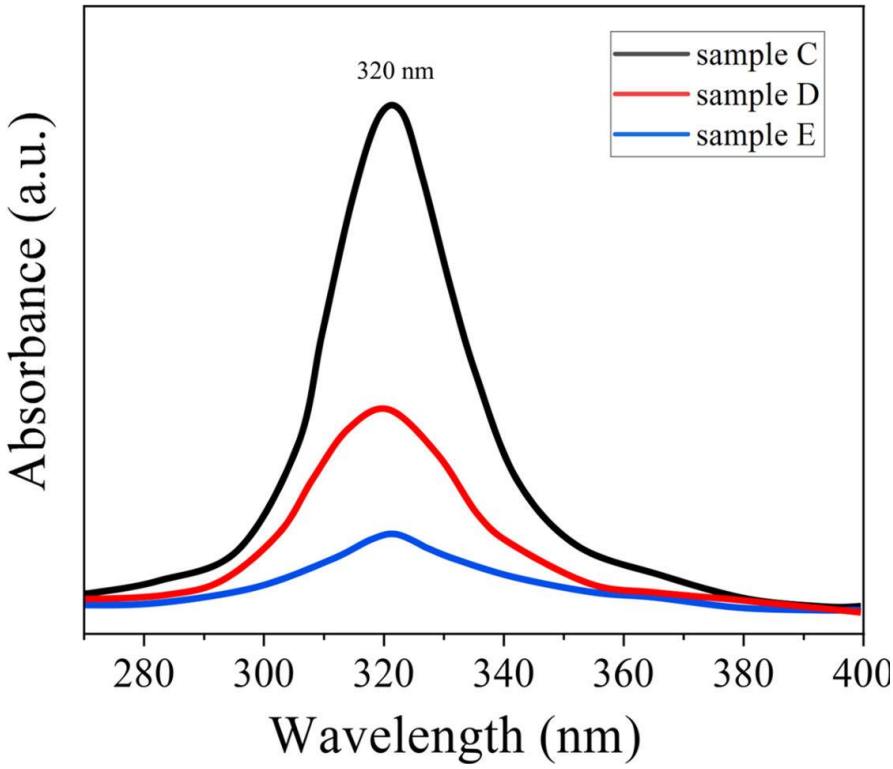

Fig. 9 Absorption spectrum of the synthesized $NaYF_4:Pr^{3+}@NaYF_4:Eu^{3+}$ core@shell nanoparticles.

The variation in optical properties caused by the shelling of $NaYF_4:Eu^{3+}$ over $NaYF_4:Pr^{3+}$ nanoparticles have been investigated by UV-Vis spectroscopy at room temperature in the wavelength range of 270 to 400 nm. The resulting absorption spectra of the prepared $NaYF_4:Pr^{3+}@NaYF_4:Eu^{3+}$ core@shell nanoparticles are shown in Fig. 9. When a photon with a greater energy than the material's bandgap energy is absorbed, an electron jumps from the valence band to the conduction band, and absorption rises abruptly. The optical bandgap corresponds to the wavelength of the absorption peak.

The existence of a single absorption band centered at 320 nm for the synthesized sample can be clearly seen in the figure 9 that may be because of the monodispersion of nanoparticles. It's worth noting that while the absorption varies in each of the three generated samples, the peak location remains consistent, demonstrating that the sol-gel process was effective in forming $NaYF_4:Pr^{3+}@NaYF_4:Eu^{3+}$ core@shell nanoparticles. It suggests that the two phosphors $NaYF_4:Eu^{3+}$ and $NaYF_4:Pr^{3+}$ are in tight contact, with band edges that are well-matched. The absorption spectrum of previous published pristine $NaYF_4:Eu^{3+}$ is different from the spectrum obtained for the synthesized $NaYF_4:Pr^{3+}@NaYF_4:Eu^{3+}$ core@shell nanoparticles indicating appropriate interactions between shell $NaYF_4:Eu^{3+}$ and core

$NaYF_4:Pr^{3+}$, resulting in a transformation of the electronic structure and optical characteristics. Moreover, photovoltaic devices might benefit from improved optical absorption in the core-shell configuration of sample C. Conclusively, it can be said that the obtained sample C of $NaYF_4:Pr^{3+}@NaYF_4:Eu^{3+}$ is expected to considerably boost the effectiveness of solar cell device by enhancing its optical properties and is therefore tested in OSC.

3.8 Solar cell characterization

After the characterization of the synthesized nanoparticles, the prepared samples were tested in solar cell devices. The techniques employed to investigate the photovoltaic characteristics of solar cells include current density- voltage (J-V) characteristics. *J-V* characteristics of the fabricated solar cells were recorded with computer controlled Keithley 2420 digital source-meter. For photovoltaic characterization, the measurement was carried out utilizing a custom-made solar simulator (Newport, Model no. 94023A) (Sol3A Class AAA Solar Simulator, Oriel, USA) under 1sun (AM1.5G), 100 mW/cm^2 illumination.

Solar conversion efficiency measurement:

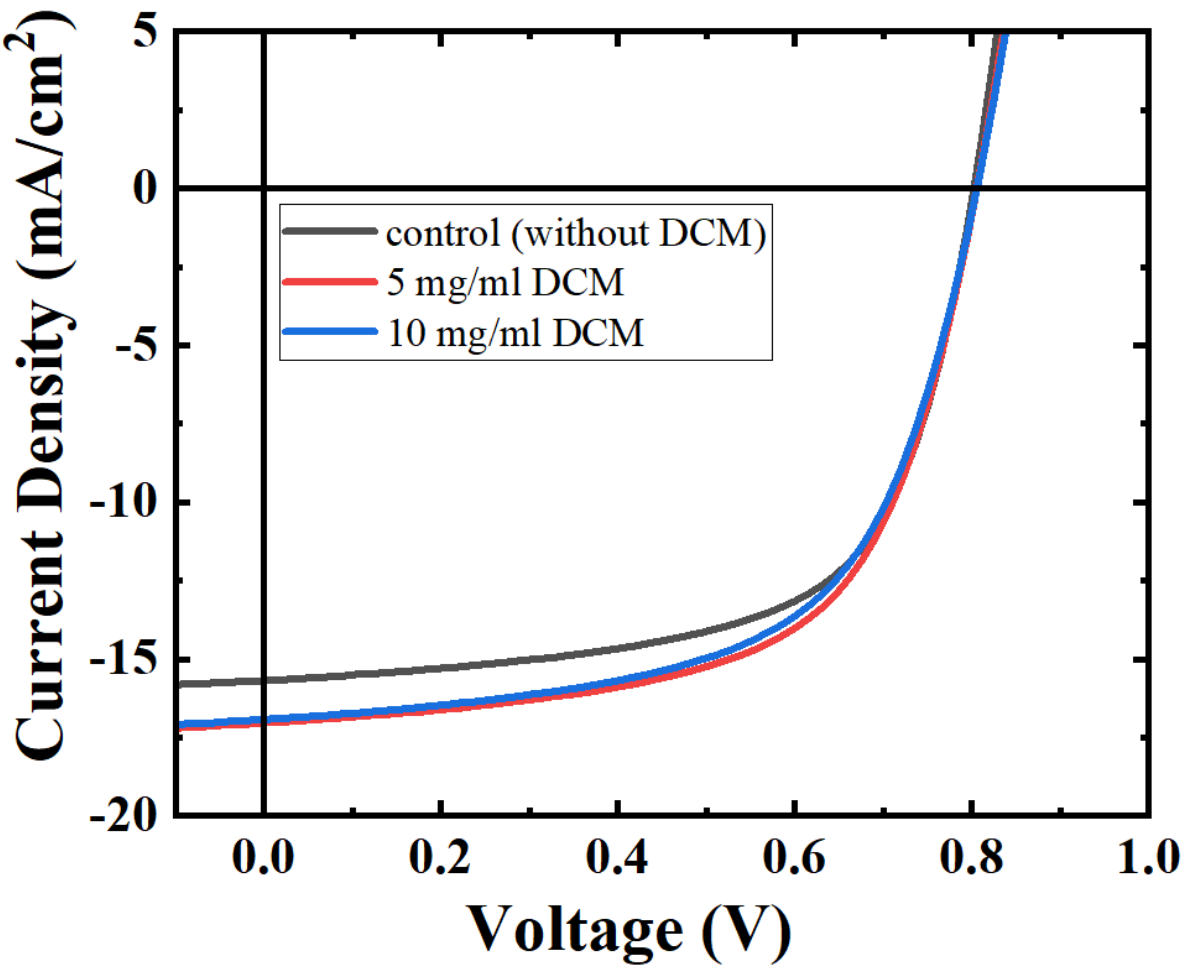

Fig. 10 J-V plot of the fabricated OSCs employing PTB7:$PC_{71}BM$ as absorber and sample C as DCM in different concentrations.

Fig. 10 shows the current J-V graphs of the fabricated OSCs with and without DCM (sample C). Photovoltaic parameters like short-circuit current density (J_{SC}), open-circuit voltage (V_{OC}), fill factor (FF), and PCE (η) of the fabricated devices are summarized in Table 1. For the control device, a V_{OC} of 0.800 V, a J_{SC} of 15.68 mA/cm^2, and a fill factor of 63.44% were obtained, which correspond to a PCE of 7.95 %. When the sample C of $NaYF_4:Pr^{3+}$@$NaYF_4:Eu^{3+}$ core@shell nanoparticles as DCM was introduced with concentration of 5 mg/ml, an 8.6 % increase in J_{SC} from 15.68 to 17.03 mA/cm^2 was attained. The better absorption is partially responsible for the increased photocurrent. Moreover, this is also due to the OSC's improved active layer structure with a flat surface as well as uniform thickness.

Table 1: Performance parameters of the fabricated OSCs employing sample C as DCM in different concentrations.

Concentration of DCM	V_{oc} (V)	J_{sc} (mA/cm^2)	FF (%)	PCE (%)
10 mg/ml	0.801	16.92	60.47	8.19
5 mg/ml	0.802	17.03	61.92	8.45
00 mg/ml	0.800	15.68	63.44	7.95

Since the DCM transforms ultraviolet radiation into visible light waves, it serves to protect the absorber structure from ultraviolet damage. The efficiency of OSC containing $NaYF_4:Pr^{3+}@NaYF_4:Eu^{3+}$ DCM layer is significantly improved than the control device due to the increased ultraviolet usage. Supplemental red photons are produced by the down-conversion material that has been swiftly absorbed by the active layer, resulting in photocurrent amplification. The portion of the ultraviolet spectrum being transformed to visible range is subsequently absorbed by the photoactive layer. [29]. Importantly, it is noticed that with the further rise in concentration (10 mg/ml) of the DCM, the J_{sc} decreased which consequently decreases the efficiency. The PCE drops since the DCM layer lowered the intensity of the incoming radiation which causes the reduction in J_{SC}. For 5 mg/ml, the results look good and promising from J-V characteristics.

Stability measurements under UV illumination:

The control device demonstrated poor stability under UV-B light, and a loss of 38% in efficiency has been seen after 90 minutes. The device with DCM (5 mg/ml) indicates comparatively high stability (Fig. 11a) and retained 84% efficiency i.e., loss of only 16% PCE. For the optimized OSCs, the J_{sc} value decreased by 3% after 30 minutes of UV illumination, validating that there is approximately no change in photocurrent (Fig. 11b). On the other hand, the J_{sc} value of control device reduces to 4% of the initial value. The J_{sc} of control OSC drops to 11% and that of device with DCM to 5% of their particular initial values after 90 minutes. It confirms that the DCM has the capability to seize the UV degradation effects and enhance the stability of the device. The V_{oc} of the two kinds of cells do not exhibit a noteworthy degradation (Fig. 11c). V_{oc} of the device with DCM dropped by just 1.9% while that of the control device by 2.8% after 90 minutes. The FF of the optimized device demonstrated better behaviour than that of the control device during continuous UV

illumination (Fig. 11d). Additionally, both the OSCs (with and without DCM) exhibit a narrow distribution, proving that the errors are diminutive, and the enhancement of PCE should come from the light conversion and UV blocking contributed by the DCM. In summary, the $NaYF_4:Pr^{3+}@NaYF_4:Eu^{3+}$ core@shell nanoparticles as down-conversion material in the OSCs are accountable for the augmentation of photocurrent density as well as the reduction of UV degradation.

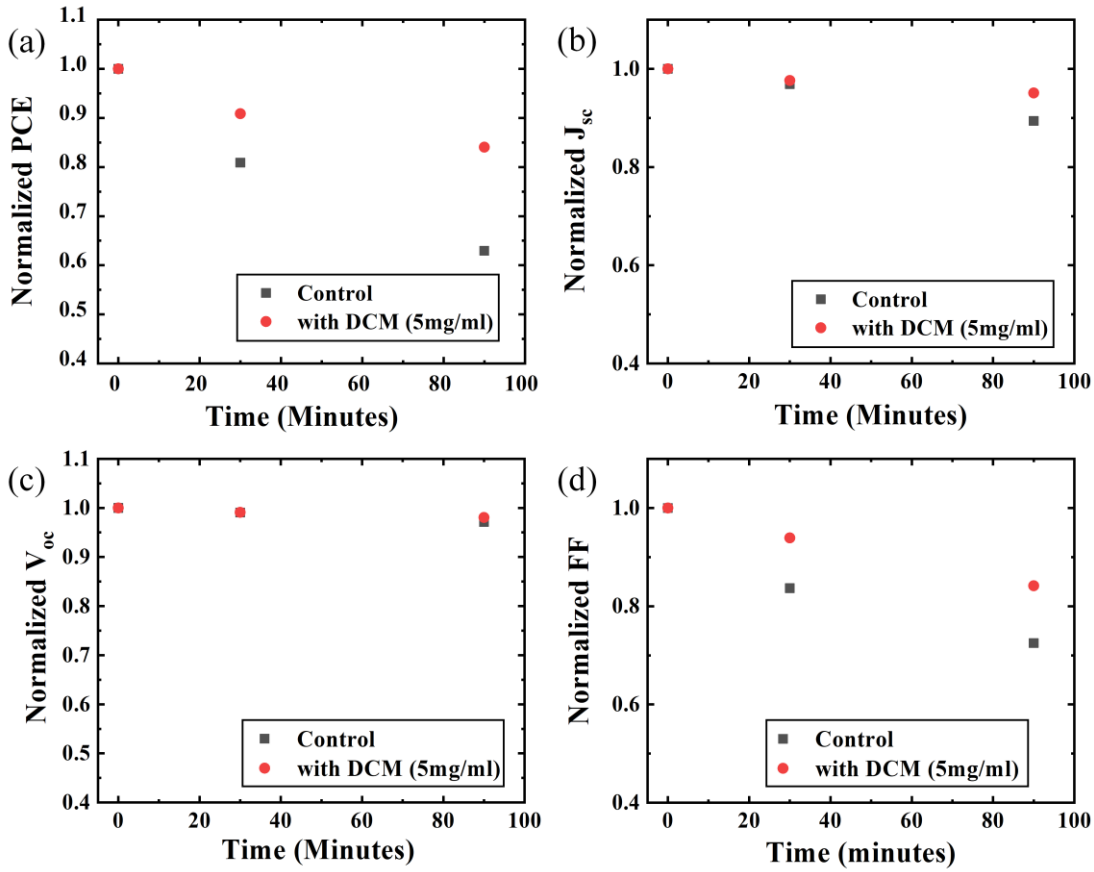

Fig. 11 Normalized stability of the fabricated OSCs with DCM (5 mg/ml) and without DCM (control).

4. Conclusions

In this work, an appropriate methodology for improving OSCs photovoltaic performance through the use of transparent luminous down-conversion material is described. The ultraviolet absorption of the DCM based on $NaYF_4:Pr^{3+}@NaYF_4:Eu^{3+}$ core@shell nanoparticles is wide, and the current findings show that dopants Pr^{3+} and Eu^{3+} based transparent luminescent layer coated over the backside of the OSCs may increase photovoltaic performance. The spectral response range of OSCs was effectively expanded to the ultraviolet

range using down conversion technology, resulting in a photocurrent gain for active OSCs. The OSC coated with DCM of $NaYF_4:Pr^{3+}$@$NaYF_4:Eu^{3+}$ core@shell nanoparticles in solvent 2-Methoxyethanol with a concentration of 5 mg/ml reaches a PCE of 8.45 %, which is approximately 6.3% higher than that of control device. Because of the efficient use of ultraviolet light, the J_{SC} of OSCs has increased dramatically from 15.68 to 17.03 mA cm^{-2}. As a result, a down-conversion material exhibiting an ideal absorption band which absorbs accessible short-wavelength ultraviolet radiation at 320 nm and consequently emits visible radiation with a spectral response which is well-matched to the OSCs might be a potential alternative to boost performance of OSCs. Our findings might open up new opportunities for improving OSCs performance as well as stability by synthesizing $NaYF_4:Pr^{3+}$@$NaYF_4:Eu^{3+}$ core@shell nanoparticles through a chemical sol-gel approach which is time-saving as well as facile.

Acknowledgments

This work was supported by the Science and Engineering Research Board (SERB), India (File no. EEQ/2021/000172).

Author contributions

Prerna Mahajan: Conceptualization, Validation, Visualization, Writing – review & editing
Anoop Singh: Conceptualization, Methodology, Analysis, Writing
Ram Datt: Characterization, Writing – review & editing
Wing Chung Tsoi: Writing – review & editing
Vinay Gupta: Writing – review & editing
Sandeep Arya: Conceptualization, Supervision, Methodology, Writing – review & editing

Conflict of Interest

The authors declare that they have no known competing financial interests or personal relationships that could have appeared to influence the work reported in this paper.

Data and code availability

The raw/processed data required to reproduce these findings will be available on the reasonable request.

Supplementary information

Not Applicable

Ethical approval

Not Applicable

References

[1] Mahajan P, Datt R, Chung Tsoi WC, Gupta V, Tomar A, Arya S (2021) Recent progress, fabrication challenges and stability issues of lead-free tin-based perovskite thin films in the field of photovoltaics. Coord Chem Rev 429:213633.

[2] Lewis NS, Nocera DG (2006) Powering the planet: Chemical challenges in solar energy utilization. Proc Natl Acad Sci U S A 103:15729-15735.

[3] Arya S, Mahajan P, Gupta R, Srivastava R, Tailor N, Satapathi S, Sumathi RR, Datt R, Gupta V (2020) A comprehensive review on synthesis and applications of single crystal perovskite halides. Prog Solid State Chem 60:100286.

[4] Mahajan P, Padha B, Verma S, Gupta V, Datt R, Tsoi WC, Satapathi S, Arya S (2022) Review of current progress in hole-transporting materials for perovskite solar cells. J Energy Chem 68:330-386.

[5] Mahajan P, Singh A, Arya S (2020) Improved performance of solution processed organic solar cells with an additive layer of sol-gel synthesized ZnO/CuO core/shell nanoparticles. J Alloys Compd 814:152292.

[6] Mahajan P, Datt R, Gupta V, Arya S (2022) Synthesis and characterization of ZnO@WO_3 core/shell nanoparticles as counter electrode for dye-sensitized solar cell. Surf Interfaces 30:101920.

[7] Mahajan P, Singh A, Datt R, Gupta V, Arya S (2020) Realization of inverted organic solar cells by using sol-gel synthesized ZnO/Y_2O_3 core/shell nanoparticles as electron transport layer. IEEE J Photovoltaics 10:1744-1749.

[8] Zheng Z, Wang J, Bi P, Ren J, Wang Y, Yang Y, Liu X, Zhang S, Hou J (2022) Tandem organic solar cell with 20.2% efficiency. Joule 6:171-184.

[9] Patel JB, Tiwana P, Seidler N, Morse GE, Lozman OR, Johnston MB, Herz LM (2019) Effect of ultraviolet radiation on organic photovoltaic materials and devices. ACS Appl Mater Interfaces 11:21543-21551.

[10] Tian C, Betancourt-Solis G, Nan Z, Liu K, Lin K, Lu J, Xie L, Echegoyen L, Wei Z. (2021) Efficient and stable inverted perovskite solar cells enabled by inhibition of self-aggregation of fullerene electron-transporting compounds. Sci Bull 66:339-346.

[11] Datt R, Bishnoi S, Lee HKH, Arya S, Gupta S, Gupta V, Tsoi WC (2022) Down-conversion materials for organic solar cells: Progress, challenges, and

perspectives: Photovoltaics: Special Issue Dedicated to Professor Yongfang Li. Aggregate 3:e185.

[12] Datt R, Bishnoi S, Hughes D, Mahajan P, Singh A, Gupta R, Arya S, Gupta V, Tsoi WC (2022) Downconversion materials for perovskite solar cells. Sol RRL 6:2200266.

[13] Shockley W, Queisser HJ (1961) Detailed balance limit of efficiency of p-n junction solar cells. J Appl Phys 32:510-519.

[14] Trupke T, Green MA, Würfel P (2002) Improving solar cell efficiencies by up-conversion of sub-band-gap light. J Appl Phys 92:4117-4122.

[15] Wang X, Sun Q, Gao J, Wang J, Xu C, Ma X, Zhang F (2021) Recent progress of organic photovoltaics with efficiency over 17%. Energies 14:4200.

[16] Datt R, Sharma R, Bishnoi S, Gupta V (2019) Förster resonance energy transfer in p-DTS(FBTTh$_2$)2-p-SIDT(FBTTh$_2$)$_2$ small molecule ternary blend bulk-heterojunction solar cells for enhanced power conversion efficiency. Mater Lett 25:122-125.

[17] Gao J, Gao W, Ma X, Hu Z, Xu C, Wang X, An Q, Yang C, Zhang X, Zhang F (2020) Over 14.5% efficiency and 71.6% fill factor of ternary organic solar cells with 300-nm thick active layers. Energy Environ Sci 13:958-967.

[18] Lodh A, Thool K, Samajdar I (2022) X-ray diffraction for the determination of residual stress of crystalline material: An overview. Trans Indian Inst Met 75:983-995.

[19] Banski M, Afzaal M, Podhorodecki A, Misiewicz J, Abdelhady AL, O'Brien P (2012) Passivation of lanthanide surface sites in sub-10 nm $NaYF_4:Eu^{3+}$ nanocrystals. J Nanopart Res 14:1−10.

[20] Jahil SS, Mohammed IA, Khazaal AR, Jasim KA, Harbbi KH (2022) Application the Halder–Wagner to calculation crystal size and microstrain by X-ray diffraction peaks analysis. NeuroQuantology 20:199-204.

[21] Dery B, Zaixiang L (2021) Scanning electron microscopy (SEM) as an effective tool for determining the morphology and mechanism of action of functional ingredients. Food Rev Int:1-20.

[22] Hong RY, Qian JZ, Cao JX 2006 Synthesis and characterization of PMMA grafted ZnO nanoparticles. Powder Technol 163:160-168.

[23] Namagal S, Jaya NV, Muralidharan M, Sumithra S (2020) Optical and magnetic properties of pure and Er, Yb-doped β-$NaYF_4$ hexagonal plates for biomedical applications. J Mater Sci Mater Electron 31:11398-11410.

[24] Gilliland GD (1997) Photoluminescence spectroscopy of crystalline semiconductors. Mater Sci Eng R Rep 18:99-399.

[25] Arya S, Prerna A, Singh A, Kour R (2019) Comparative study of CuO, CuO@Ag and CuO@Ag:La nanoparticles for their photosensing properties. Mater Res Express 6:116313.

[26] Singh A, Arya S, Khanuja M, Hafiz AK, Datt R, Gupta V, Khosla A (2020) Eu doped $NaYF_4$@Er: TiO_2 nanoparticles for tunable ultraviolet light based anticounterfeiting applications. Microsyst Technol:1-10.

[27] Stouwdam JW, Raudsepp M, Van Veggel FC (2005) Colloidal nanoparticles of Ln^{3+}-doped $LaVO_4$: Energy transfer to visible- and near-infrared-emitting lanthanide ions. Langmuir 21:7003-7008.

[28] Jiang L, Chen W, Zheng J, Zhu L, Mo LE, Li Z, Hu L, Hayat T, Alsaedi A, Zhang C, Dai S (2017) Enhancing the photovoltaic performance of perovskite solar cells with a down-conversion Eu-complex. ACS Appl Mater Interfaces 9:26958-26964.

[29] Huang CK, Chen YC, Hung WB, Chen TM, Sun KW, Chang W-L (2013) Enhanced light harvesting of Si solar cells via luminescent down-shifting using YVO4: Bi^{3+}, Eu^{3+} nanophosphors. Prog Photovolt Res Appl 21:1507-1513.